The impact of tides on simulated landfast ice in a pan-Arctic ice-ocean model

Jean-François Lemieux [1], Ji Lei [2], Frédéric Dupont [2], François Roy [1], Martin Losch [3], Camille Lique [4], Frédéric Laliberté [5]

[1]Recherche en Prévision Numérique Environnementale/Environnement et Changement Climatique Canada, 2121 route Transcanadienne, Dorval, Qc, Canada.
[2]Service Météorologique Canadien, Environnement et Changement Climatique Canada, 2121 route Transcanadienne, Dorval, Qc, Canada.
[3]Alfred-Wegener-Institut, Helmholtz-Zentrum für Polar- und Meeresforschung, Postfach 120161, 27515 Bremerhaven,Germany
[4]Laboratoire d'Océanographie Physique et Spatiale (LOPS), CNRS, IRD, Ifremer, IUEM, 29280, Brest, France
[5]Climate Research Division, Environment and Climate Change Canada, Toronto, On, Canada

Key Points:

- Tides decreases the extent of simulated landfast ice in tidally active regions
- Simulated landfast ice is more in line with the observations
- The lower extent of landfast ice is dynamically driven by the ocean stress on the ice

Corresponding author: J-F. Lemieux, `jean-francois.lemieux@canada.ca`

Abstract

Most sea ice models poorly simulate the landfast ice cover. This is often due to an underestimation of ice arching and the lack of a parameterization to represent the grounding of pressure ridges in shallow water. Recent work has shown that a modified sea ice rheology and the addition of a grounding scheme notably improve the simulation of landfast ice in regions such as the East Siberian Sea, the Laptev Sea, the Kara Sea and along the Alaskan coast. However, these numerical experiments indicate there is an overestimation of the extent of landfast ice in regions of strong tides such as the Gulf of Boothia, Prince Regent Inlet and Lancaster Sound. In this study, pan-Arctic simulations are conducted with an ice-ocean (CICE-NEMO) model with a modified rheology and a grounding scheme. We study the impact of tides on the simulated landfast ice cover. Results show that tides clearly decrease the extent of landfast ice in some tidally active regions. Thermodynamics and changes in grounding cannot explain the lower landfast ice area due to tides. We rather demonstrate that this decrease in the landfast ice extent is dynamically driven by the increase of the ocean-ice stress due to the tides.

1 Introduction

Immobile or almost immobile sea ice located near a coast is often referred to as landfast ice. Landfast ice is observed in many coastal regions of the Arctic [*Yu et al.*, 2014] and of the Antarctic [*Nihashi and Ohshima*, 2015]. In the Arctic (the region of interest in this paper), large extents (up to hundreds of km into the sea) of landfast ice are observed in winter and spring in the East Siberian, the Laptev and the Kara Seas. In the Laptev Sea, grounded pressure ridges have been observed and identified as anchor points for the stabilization of the landfast ice cover [*Haas et al.*, 2005; *Selyuzhenok et al.*, 2017]. Modeling experiments suggest that grounding is also an important mechanism for the presence of landfast ice in the East Siberian Sea [*Lemieux et al.*, 2015, 2016; *Losch and Lemieux*, submitted]. As the Kara Sea is overall deeper than the East Siberian and Laptev Seas, grounding is less effective and it is thought that a series of islands act as pinning points for stabilizing its landfast ice cover [*Divine et al.*, 2005; *Olason*, 2016; *Losch and Lemieux*, submitted]. In the Chukchi and Beaufort Seas, where the continental shelves are narrower than in the East Siberian and Laptev Seas, the landfast ice cover can extend a few tens of km away from the coast. Grounding is again an important physical process for explaining the presence of landfast ice in these regions [*Mahoney et al.*, 2007, 2014]. Landfast ice is also present off the east coast of Greenland, in some coastal regions of Baffin Bay and Hudson Bay and in many inlets and channels of the Canadian Arctic Archipelago (CAA) where the ice is landlocked.

Landfast ice has an important impact on ocean-ice-atmosphere interactions. Indeed, as it is immobile, it decreases the transfer of heat, moisture and momentum between the atmosphere and the ocean. The offshore edge of landfast ice often exhibits polynyas that can be important sites for the formation of new sea ice [*Dethleff et al.*, 1998]. It has also been shown that the landfast ice cover off the Siberian shelf plays a role in the formation of the Arctic cold halocline layer [*Itkin et al.*, 2015]. The presence of landfast ice can, locally, strongly modulate the mean and the structure of the ocean flow through narrow straits such as Nares Strait [*Rabe et al.*, 2012].

Due to their low spatial resolutions and the lack of representation of some physical mechanisms such as grounding, sea ice models usually poorly simulate the landfast ice cover [*Johnson et al.*, 2012; *Laliberté et al.*, submitted]. With the increase in spatial resolution of ice-ocean forecasting systems and even of climate models, there is growing interest in better representing the formation, stabilization and break up of landfast ice. Hence, over the past few years, some modelers have modified the sea ice rheology and have developed parameterizations to better simulate landfast ice. *Dumont et al.* [2009] studied the impact of the ellipse aspect ratio of the standard viscous-plastic (VP) rheology on the simulation of the North Water Polynya ice bridge. In order to model landfast ice, *König Beatty and Holland* [2010] introduced a simple formulation for adding isotropic tensile strength to the standard VP rheology. *Itkin et al.* [2015] increased the ice strength in shallow regions in order to better simulate landfast ice. *Olason* [2016] studied the impact of some physical and numerical parameters of a VP model on the simulated landfast ice in the Kara Sea. *Rallabandi et al.* [2017] developed an analytical theory of the flow of sea ice through narrow straits and on the formation of ice bridges. *Dansereau et al.* [2017] investigated the simulation of ice bridges with the new Maxwell-elasto-brittle rheology. To represent grounding in shallow water, *Lieser* [2004] proposed a simple approach to set the ice at rest in shallow water. Following the work of *Lieser* [2004], *Lemieux et al.* [2015] introduced a parameterization that represents the seabed (or basal) stress in the momentum equation due to grounded ice ridges. *Losch and Lemieux* [submitted] showed that the extent of landfast ice increases as the grid is refined due to a larger effective shear strength at higher resolution.

Recently, it was shown that landfast ice in the Arctic can be reasonably well simulated by using a grounding scheme and a modified VP rheology [*Lemieux et al.*, 2016]. However, Fig. 8 in *Lemieux et al.* [2016] indicates that the model clearly overestimates the presence of landfast ice in the Gulf of Boothia, Prince Regent Inlet, Lancaster Sound and to a lesser extent in Foxe Basin. Interestingly, these regions are known to experience strong tidal forcing. The same conclusions can be drawn from the results of *Losch and Lemieux* [submitted]. As tides were not included in the ice-ocean simulations of *Lemieux et al.* [2016] and of *Losch and Lemieux* [submitted], this overestimation could be due to the absence of this forcing.

Apart from these tidally active regions in Canadian waters, most of the Arctic Basin lies poleward of the critical latitude (74.5° N) beyond which waves at the dominant semi-diurnal (M2) tidal frequency still propagate but not as freely due to the higher value of the inertial frequency [*Rippeth et al.*, 2015]. Even though the tides are in general of small amplitude in the Arctic, they can be significant in specific regions such as the White Sea and the Barents Sea. In the latter region, tides are an important source of energy dissipation and control part of the heat loss from the Atlantic Water to the atmosphere and the dense water formation [*Årthun et al.*, 2011]. These water mass transformations are important as they might determine the location of the ice edge. More generally, tidal motion also has a direct dynamical impact on sea ice as it generates divergence-convergence cycles that affect the sea ice growth and melting [*Koentopp et al.*, 2005]. Finally, tides are thought to play a role in the formation and maintenance of some Arctic polynyas [*Hannah et al.*, 2009].

In this paper, we will show that including tides notably decreases the simulated area of landfast ice in regions such as Gulf of Boothia, Prince Regent Inlet, Lancaster Sound, Nares Strait and Foxe Basin. The objectives of this paper are to investigate the impact of the tides on the simulated landfast ice cover and to identify mechanisms related to tides that lead to such a lower extended landfast ice cover in these regions. The focus is on the impact of tides on the simulated landfast ice, not the opposite. Some authors have studied the impact of tides on the simulated pack ice (e.g. *Koentopp et al.* [2005], *Holloway and Proshutinsky* [2007], *Årthun et al.* [2011], *Luneva et al.* [2015]) but it is, to our knowledge, the first time that a numerical study focuses on the influence of tides on landfast ice.

This paper is structured as follow. In section 2, the ice-ocean model is introduced and the experimental setup is described. Observations used for the validation are presented in section 3. The main results are presented in section 4. Concluding remarks are provided in section 5.

2 Experimental setup

A pan-Arctic ice-ocean model is used to conduct two 10 year simulations (1 October 2001 - 31 December 2010): one with 'no tides', referred to as NT and one with 'tides' referred to as T. The sea ice model is CICE version 4.0 [*Hunke and Lipscomb*, 2008] with some modifications that include the UK Met Office CICE-NEMO interface [*Megann et al.*, 2014], the grounding scheme of *Lemieux et al.* [2015] and a modified VP rheology as described in [*Lemieux et al.*, 2016]. CICE uses an ice thickness distribution (ITD) model, here with 10 thickness categories (as defined in *Smith et al.* [2016]). Following *Lemieux et al.* [2016], the basal stress parameters are k_1=8 and k_2 =15 Nm^{-3} and the standard VP rheology is modified by setting the ellipse aspect ratio to 1.4 and by adding a small amount of isotropic tensile strength (k_t=0.05). The advective time step Δt is 10 min. For a better numerical convergence of the Elastic-VP (EVP) solver we used a larger number (920) of subcycling iterations (N_{sub}) than the default value (120).

The ocean model is NEMO version 3.6 [*Madec*, 2008] applied in a variable volume and nonlinear free surface configuration. Ocean mixing is parameterized with the Turbulent Kinetic Energy (TKE) scheme. 75 vertical ocean levels are used. As for the sea ice model, the ocean time step is 10 min. The formulation of the drag coefficients is described in *Roy et al.* [2015].

Our 0.25° grid covers the Arctic, the North Atlantic and the North Pacific (it is an extended version of the grid used by *Lemieux et al.* [2016] which did not include the Pacific portion). This subset of the 0.25° global ORCA mesh has a spatial resolution of ∼12.5 km in the central Arctic. We focus on the Arctic Ocean and Canadian waters (see Figure 1 for the region of interest).

The ice-ocean simulations are forced by 33 km resolution atmospheric reforecasts from Environment and Climate Change Canada (ECCC, *Smith et al.* [2014]). The simulations were initialized with average (September-October 2001) sea ice concentration from the National Snow and Ice Data Center (NSIDC, http://nsidc.org/data/seaice_index/) and the average (October-November 2003) sea ice thickness field derived from ICESat

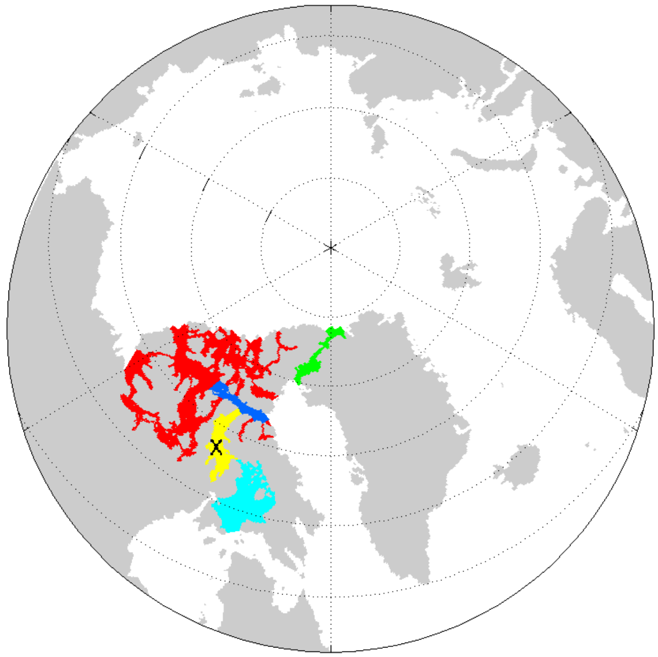

Figure 1. Part of the domain analyzed. Four regions with strong tides are defined and respectively referred to as: Nares in green, Lancaster in blue, Boothia in yellow and Foxe Basin in cyan. An additional region, where the impact of tides on the landfast ice cover is less important, is referred to as the 'rest of the CAA' in red. The black cross identifies a point in the Gulf of Boothia used for time series. In this paper, we refer to subregions Nares, Lancaster, Boothia and Foxe Basin as the tidally active regions.

data (https://nsidc.org/data/icesat). Initial conditions for the ocean temperature and salinity are averages (September-October) WOA13_95A4 [*Locarnini et al.*, 2013; *Zweng et al.*, 2013] fields. The ocean starts at rest (with the sea surface height field and currents set to zero). For the two open boundaries (north Pacific and north Atlantic), a monthly averaged circulation taken from the GLORYS2 version 4 reanalysis [*Garric et al.*, 2017], providing vertical profiles of ocean currents, temperature and salinity is applied. The non-linear free surface (including the tides) is treated following a time-splitting technique with a sub time step of 20 s. Vertically averaged velocities (13 harmonic components) were extracted from the solution of the Oregon State University (OSU) tidal prediction model [*Egbert and Erofeeva*, 2002]. For the open boundaries the barotropic velocity components are prescribed as in *Flather* [1976]. The tidal potential over the model domain is also considered as a sea surface height forcing term, including a correction for the self-attraction and loading effect.

The 0.25° CICE-NEMO configuration used for this paper is a testing platform for the 1/12° short-term regional ice ocean prediction system (RIOPS) now running operationally. When implementing the tides in RIOPS, we noticed that the sea ice thickness field exhibited unrealistic values (more than 10 m) at the end of the growth season in some tidally active regions. Our investigation pointed out that the ice was too weak in these regions when using the ice strength parameterization of *Rothrock* [1975] (with modifications by *Lipscomb et al.* [2007]). This problem was mitigated by using the ice strength parameterization of *Hibler* [1979]. This result is in a sense consistent with the study of *Ungermann et al.* [2017] who showed that pan-Arctic ice-ocean simulations are closer to observations when using the formulation of *Hibler* [1979] rather than the one of *Rothrock* [1975]. Hence, for the experiments described in this paper, the Hibler parameterization was used with the ice strength parameter (P^*) equal to the widely used value of 27.5 Nm^{-2}. The other CICE physical parameters are set to the default values [*Hunke and Lipscomb*, 2008].

Figure 2 compares the simulated and OSU reconstructed amplitude and phase for the two most important harmonics (M2 and K1). The amphidromes are located closely to the observed ones and the amplitudes are in general comparable to the ones in the observations. These harmonics mostly exhibit large amplitudes in Canadian waters (e.g. Foxe Basin).

3 Description of observations and methodology

The National Ice Center (NIC) 25 km gridded landfast ice product [*National Ice Center*, 2006, updated 2009] is used for validation. These bi-weekly pan-Arctic analyses, manually produced, identify grid cells that are covered by landfast ice. To compare the simulations to the NIC analyses, we follow most of the methodology of *Lemieux et al.* [2016]. Hence, the NIC landfast ice observations are interpolated to the model grid by doing a nearest grid point interpolation.

The period from October 2001 to September 2004 is used for the spinup of the simulations while the rest (until 31 December 2010) is used for the analyses. However, as the NIC landfast ice data ends in 2007, we focus on the period September 2004 to September 2007. For the simulations, daily averaged gridded outputs (defined at the tracer point) are saved. Simulated ice at a certain grid cell is considered landfast if its 2 week mean daily speed is smaller than 5×10^{-4} m s^{-1}. The area of landfast ice in a particular region is calculated by summing the area of landfast cells. Subregions (shown in Figure 1) are used to characterize the effect of tides on landfast ice in specific geographical areas. We also use the daily outputs to calculate the mean (of various variables) at each grid cell between January and May for the three year period (September 2004 to September 2007), in order to concentrate on the core of the landfast ice season.

To have a better understanding of the impact of high frequency forcing (i.e., the tides) on the sea ice cover, hourly outputs are also saved and analyzed for a shorter period (20 October 2005 - 15 June 2006). Using these outputs, we choose a point in the middle of the Gulf of Boothia and compare the T and NT simulations.

4 Results

Following *Laliberté et al.* [submitted], we calculated the average number of months of landfast ice (per year) at each grid point for the NIC observations (N_{obs}) and the simulations (N_T and N_{NT}). The fields N_{obs}, N_T and N_{NT} were calculated for the period September 2004 to September 2007. Figure 3a shows the number of months per year of landfast ice based on the NIC analyses (N_{obs}). Similarly, the number of months for the NT simulation (b) and the T simulation (c) are also displayed. The last panel (d) of this figure is the difference between the T and NT simulations (i.e. $N_T - N_{NT}$).

The number of months of landfast ice in the NT simulation is close to the number of months in the NIC analyses in coastal regions of the Arctic Ocean and in the Western part of the CAA. However, the NT simulation clearly overestimates the duration of landfast ice in the northern part of the CAA and in tidally active regions. In the northern CAA, the overestimation is due to the fact that some landfast ice survives the whole summer. Note that multi-year landfast ice is rare but is sometimes observed in some channels of the CAA (e.g. Sverdrup channel, *Serson* [1974]). In regions such as the Gulf of Boothia, Prince Regent Inlet and Lancaster Sound, however, the reason for the overestimation of the number of months in the NT simulation is different. Indeed, in these tidally active regions, the NT simulation exhibits an extended landfast ice cover in winter and spring while this is not observed.

Compared to the NT simulation, the number of months of landfast ice is notably reduced in the T simulation in the regions of strong tides. This suggests that, to the first order, the impact of tides on the landfast ice cover is local. For most of these tidally active regions, including the tides improves the simulation of landfast ice. Nevertheless, although the landfast ice is better simulated in Lancaster Sound when including the tides, there is too little landfast ice in Barrow Strait. There is even a double-arch feature in Barrow Strait (Figure 3c) that is not present in the NIC analyses (Figure 3a). A few small polynyas (e.g. in Penny Strait) can be seen in the T simulation while they are not present in the NT one (Figure 3, see also Figure 8).

Including the tides also has a strong impact in Nares Strait where the NT simulation overestimates the number of months of landfast ice while the T simulation leads to an underestimation. In fact, the ice bridge does not form anymore when the tides are included. As the largest differences between the NT and T simulations are found in tidally active regions in Canadian waters and in Nares Strait, we will pay a particular attention to these regions.

To quantify if the tides overall improve the simulation of landfast ice, we have first defined four subregions (shown in Figure 1) based on the largest negative differences in Figure 3d (by visual inspection). We refer here to these subregions as the tidally active regions. An additional subregion (rest of CAA), where the differences are smaller, is also defined. We then calculated, for these subregions, the mean error defined as $\mathcal{E} = \frac{1}{S_{tot}} \sum_{i=1}^{n} \left| N_s^i - N_{obs}^i \right| S^i$ where the summation is performed over the n ocean cells of a given subregion, the superscript i refers to these ocean cells, S^i is the surface area of the ocean cell i, S_{tot} is the total ocean area of the subregion and N_s is either N_{NT} or N_T. Table 1 gives the mean error results for the different subregions. The T simulation leads to notable improvements in the number of months of landfast ice simulated in all the subregions. The improvement is particularly remarkable in the Boothia subregion (in yellow in Figure 1) as the mean error $\mathcal{E}$ drops from 3.69 months in the NT simulation to 2.09 months when including the tides.

To further illustrate the impact of the tides, Figure 4 shows the area of landfast ice in the tidally active region Boothia (in yellow in Figure 1). Six years of simulations are shown (September 2004 -September 2010) along with the NIC observations from September 2004 to the last analysis available (31 December 2007). For the first three years, the NT simulation clearly overestimates the area of landfast ice compared to the NIC analyses. Also, the landfast area for the NT simulation saturates at the end of each landfast ice season. This is due to the fact that, inconsistent with observations, region Boothia

Region	**NT**	**T**
Nares Strait	4.59	3.44
Lancaster-Barrow	3.52	2.64
Boothia	3.69	2.09
Foxe Basin	1.85	1.01
rest of CAA	1.73	1.68
All regions	2.20	1.74

Table 1. Mean error of the number of months of landfast ice for different subregions for the NT and T simulations.

is fully covered with landfast ice. To the contrary, the T simulation does not have region Boothia fully covered by landfast ice and it is more in line with the observations. There is, however, an increase in the observed landfast ice area at the end of March 2007. The landfast ice cover stays quite extended up to the end of the landfast ice season. This is not captured by the T simulation. This is, however, exceptional for the observed landfast ice extent in this region. Indeed, in 10 years of observations (1997-2007), it is the only period with such an extended landfast ice cover in this region (not shown).

To understand what causes the overall lower presence of landfast ice in the T simulations compared to the NT one, we investigate the changes in sea ice conditions, in grounding and in the forcing. We also examine whether the reduction in landfast ice when including the tides is dynamically and/or thermodynamically driven.

First, in Figure 5, we look at the differences in the ice volume per m^2 (in other words the mean thickness in a grid cell, simply referred to as the thickness). The thickness field is the January-May mean (for the period September 2004 to September 2007). In the Arctic Ocean, the thickness fields are very similar in the T and NT simulations (slightly thicker in the T simulation). The largest differences between the T and NT simulations are in the southern Gulf of Boothia, the southern part of Foxe Basin and in Hudson Strait (Figure 5b). Overall, in these tidally active regions, the ice is clearly thicker. Time series of the total volume of sea ice in the domain in our NT and T simulations do not exhibit large differences (not shown). In winter, there is more volume in T than in NT (as seen in Figure 5b) while it is the opposite in summer. This indicates that the higher sea ice growth in the T simulation is compensated by a larger summer melt. This is different than the notable lower volume in the T simulation of *Luneva et al.* [2015] with a LIM2-NEMO coupled model. It is unclear why a different behavior is obtained here.

As the ice is thicker in the T simulation (in tidally active regions), this might suggest that grounding is more effective. This would, however, contradict the lower extent of landfast ice in the T simulation in the tidally active region. Figure 6a shows the magnitude of the basal stress (associated with grounding, *Lemieux et al.* [2015]) for the NT simulation. This figure indicates that grounding is an important mechanism mainly along the Russian and Alaskan coasts. Because Nares Strait and most channels of the CAA are relatively deep (not shown), grounding is not an important process in these regions. Apart from the eastern part of Foxe Basin where the increase in grounding in the T simulation is obvious, the other regions of the CAA show no increase (too deep) or a small increase of the basal stress due to an overall thicker ice cover (Figure 6b). Hence, changes in grounding can certainly not explain the lower extent of landfast ice in the T simulation compared to the NT one; in fact the slight increase in grounding in the T simulation should favor the formation/stabilization of landfast ice.

The fact that the ice is overall thicker in tidally active regions in the T simulation (Figure 5b) indicates that the ice cover is more active and leads to more ice production. This can be seen in the January-May mean (absolute) divergence field (Figure 7) and in the January-May mean ice concentration (Figure 8). The large extents of landfast ice (Russian Coast and CAA) are clearly visible in the absolute divergence field of the NT simulation (Figure 7a). Figure 7b (T-NT) indicates that the ice is indeed more active in regions with strong tides in the CAA, Nares Strait, Foxe Basin and Hudson Strait. Note that the difference between the T and NT mean absolute divergence fields can be expected to be larger if higher frequency outputs were used, instead of daily means. Monthly mean spatial averages of the thermodynamic ice growth/melt (not shown) exhibit a similar qualitative behavior for the four tidally active subregions: there is more growth in the T simulation than in the NT one during the growth season, because the more mobile ice creates more open water, while there is more melt during the melt season in T than in NT, probably because of an ice-albedo feedback: there is more open water due to ice mobility and hence more shortwave absorption. The larger growth in T compared to NT in all these subregions is an integrated result; this is not true at all the points of these subregions. For example, the southernmost part of the Boothia region in the T simulation exhibits thicker ice, a slightly larger number of months of landfast ice and less thermodynamical growth than in the NT simulation.

As the ice strength based on Hibler's parameterization strongly decreases with the ice concentration, the ice strength is overall reduced in most of the tidally active regions (not shown). Two exceptions are the southern Gulf of Boothia and the southern part of Foxe Basin. The increase in the ice strength in these regions is associated with thicker sea ice (Figure 5) and compact ice conditions (Figure 8).

We claim that the lower extent of landfast ice in the T simulation (in tidally active regions) is largely dynamically driven by the ocean stress at the ice interface (i.e., the ocean-ice stress simply referred to as the ocean stress in this paper). Although the difference (T-NT) of the mean (January-May) amplitude of the ocean stress clearly indicates it is larger in T than in NT in tidally active regions (not shown), a more interesting and complete view of the impact of the tidal forcing on the sea ice cover is provided by calculating the rate of change of sea ice kinetic energy (KE) per unit area.

Following *Bouchat and Tremblay* [2014], we computed the scalar product of the ice velocity vector and the different terms in the momentum equation. Figure 9 shows the January-May 2006 mean rate of change of sea ice KE due to the atmospheric stress (E_{ai}), the ocean stress (E_{oi}) and the rheology term (E_r). In the NT simulation, the ocean stress (Figure 9c) and the rheology term (Figure 9e) dissipate KE almost everywhere in the domain; the KE input being provided by the wind stress term (Figure 9a). The regions of landfast ice are easily recognizable with values of E_{ai}, E_{oi} and E_r close to 0 Wm^{-2}. As the state of stress is in the viscous regime when the ice is landfast, the very small E_r in these regions is consistent with the conclusions of *Bouchat and Tremblay* [2014], i.e. that the KE dissipated by the viscous regime is small and represents a negligible fraction of the total KE dissipated. Over most of the domain, E_{oi} and E_r in the T simulation (Figure 9d and f) are similar to the ones of the NT simulation. However, in regions of strong tides, the differences between the T and NT simulations are striking. In Foxe Basin, Nares Strait, the Gulf of Boothia and Prince Regent Inlet, the ocean stress term does not dissipate KE but to the contrary is a source of KE; it clearly acts to set the ice in motion. Moreover, E_{oi} is generally much larger than the rate of KE input due to the wind in these regions (Figure 9b). These zones of positive E_{oi} in the T simulation are very well spatially correlated with zones of negative E_r. This means that the ocean stress term in these tidally active regions increases the KE of the ice with a notable fraction of it being dissipated by the rheology term (by plastic deformations).

Following *Koentopp et al.* [2005], we use high-frequency outputs (hourly) to plot various time series at a point to gain further insight into the effect of the tides on the ice cover. This point is located in the Gulf of Boothia and is marked by a cross in the yellow region of Figure 1. The time series start on 20 October 2005 and ends up on 15 June 2006. Note that we looked at other points, in all four tidally active regions, where the number of months of landfast ice is clearly lower in T than in NT and we found qualitatively similar behaviors as what is described below for the point in the Gulf of Boothia.

Large wind stress events at the beginning of the period (October-November 2005) increase the KE at this point in both simulations (Figure 10a). This leads to strong losses of KE due to the ocean stress term (Figure 10b). Both simulations exhibit an active ice cover at this point (Figure 10d). Starting in December, the NT simulation is almost always at rest; it exhibits a few episodes with a small non-zero ice speed. The last one occurs at the end of January and it is associated with a large wind stress event (Figure 10a). This is the same event indicated by the black arrow in Figure 4. After this strong wind event, the ice in the NT simulation is landfast at this point up until the end of our high-frequency record. In the T simulation, the same point is never landfast and exhibits an ice speed that is clearly related to the tidal forcing (semidiurnal, diurnal and $\sim$14 day spring-neap oscillation). From the end of November 2005 to the end of May 2006, the ocean stress term is always a source of KE at this point in the T simulation. Interestingly, while the wind stress in the NT simulation is either zero or a source of KE, the wind stress in the T simulation can be a source or lead to a loss of KE (depending whether the wind is in the direction or in the opposite direction of the ice velocity vector). The rheology term dissipates quite a lot of KE in the T simulation except at the beginning and at the end of the period shown (because the ice strength is then very small, Figure 11c).

In the NT simulation, the ice concentration is close to 1 at the end of November 2005 and stays like this up until May 2006 (Figure 11a). In the time series for the T simulation, the ice concentration shows a lot more variability as the ice is still active. The thicker ice in T than in NT suggests there is more ice production in the T simulation than in the NT one (Figure 11b). The ice strength in the T time series 'oscillates around' the NT one. On average, the ice strengths are similar because the decrease due to the lower ice concentration in the T time series is compensated by a higher thickness. Even when there are episodes for which the ice strength in the T simulation is larger than in the NT one, the ice is not fast due to the much larger ocean stress at the ice interface.

Another striking difference in the two time series is the behavior of the ice concentration and thickness in May 2006 (Figure 11a and b). The ice concentration and thickness start to decrease at the beginning of May in T while this happens at the end of the month for the NT time series. This is likely a consequence of the ice-albedo feedback (more absorption of solar radiation) due to the already slightly lower concentration at the beginning of May and the more active ice cover and possibly larger ocean heat fluxes (this would require further investigation).

Time series of the ice growth at this specific point (not shown) are consistent with what was previously mentioned: there is more ice formation in T than in NT. Temperature and salinity profiles at this location also help to understand the interactions between the ocean and the sea ice (Figure 12). At the beginning of the period on 20 October 2005, the vertical structure of the temperature and salinity profiles in T are similar to the ones in NT. The profiles on 3 May 2006 indicate there is a lot more vertical mixing in T than in NT. The fact that the warm layer bellow the mixed layer is eroded in T compared to NT (Figure 12a) suggests there are larger vertical heat fluxes in T in winter at the ice underside but that this is more than compensated by increased heat loss to the atmosphere (consistent with more ice growth). The saltier mixed layer in T compared to NT could also be evidence of a greater ice production (due to salt rejection).

5 Concluding remarks

This paper addresses the following questions: 1) what is the impact of tides on the simulated landfast ice cover? 2) which physical mechanism(s) are involved?

Using a 0.25° pan-Arctic ice-ocean model, a simulation without tides (NT) and a simulation with 13 tidal constituents (T) were conducted. When including the tides, the simulated landfast ice cover is strongly modified in tidally active regions; the area of simulated landfast ice is notably reduced and usually more in line with the observations. The most striking differences are found in the Gulf of Boothia, Prince Regent Inlet, Lancaster Sound, Foxe Basin and in Nares Strait. The impact of tides on the landfast ice cover is mostly a local phenomenon; in regions with weak tidal forcing, the landfast ice cover in the T simulation is similar to the one in the NT simulation.

We demonstrate that the first order mechanism responsible for the lower extent of landfast ice in tidally active regions is the much larger ocean-ice stress in the T simulation than in the NT one. While, on average (January-May), the ocean stress dissipates ice kinetic energy (KE) everywhere on the domain in the NT simulation, the situation is very different in tidally active regions in the T simulation. Indeed, in these regions, the ocean stress is usually a source of sea ice KE; the largest inputs of KE by the ocean stress are on average found in Foxe Basin, Gulf of Boothia and Nares Strait. Moreover, in these regions, the rate of KE input is usually larger for the ocean stress term than for the wind stress. Also, in these regions, a notable fraction of the KE is dissipated by the sea ice rheology term (by plastic deformations). This is again a remarkable difference between the NT and T simulations.

These plastic deformations are characterized by a regular divergence-convergence (often with shear) cycle. On average (January-May) the ice concentration is lower in the T simulation than in the NT one in tidally active regions (with very small differences in the Arctic Ocean). These frequent openings in the sea ice cover lead to a higher production of new sea ice in the T simulation than in the NT one (mostly in Canadian waters). This is an indication that the lower extent of landfast ice in the T simulation compared to the NT one is not thermodynamically driven; the thicker ice in the T simulation should favor the formation/stabilization of a landfast ice cover.

In the simulations described here, constant atmospheric and oceanic neutral drag coefficients were used following the formulation of *Roy et al.* [2015]. We speculate that the processes described above could even be more important if form drag [*Tsamados et al.*, 2014] was also considered. Essentially, we argue that the tidally induced divergence-convergence cycle which leads to thicker ice in winter should increase the form drag and therefore further increase the ocean stress at the ice interface. This potential positive feedback mechanism would require to be investigated in an ice-ocean model that includes the effect of form drag.

Because the ice is usually thicker in tidally active regions in the T simulation than in the NT one, there is more grounding. However, this occurs over a few small regions (mostly in the southern part of the Gulf of Boothia and in the eastern part of Foxe Basin) as most channels and inlets are too deep for pressure ridges to reach the seafloor. In fact, in the CAA and in Nares Strait, grounding is not an important mechanism for the formation and stabilization of the landfast ice cover.

Although the simulation with tides leads to an overall better landfast ice cover than the NT experiment, the region of Barrow Strait is an exception. Indeed, compared to observations, the region free of landfast ice in this section of the Northwest passage extends too far west. Another interesting point about our simulations is the change in the landfast ice conditions in Nares Strait. In the NT simulation, the average number of months of landfast indicate there is an ice bridge that sometimes form in Nares Strait while the ice bridge does not exist in the T simulation. Compared to the observations, the NT simulation overestimates the number of months of landfast ice while it is the opposite for the simulation with tides. These results suggest that some models might be able to simulate the North Water Polynya ice bridge and landfast ice in some regions of the Canadian Arctic Archipelago due to a compensation of errors; the ice is too thin or too weak but the model still simulates landfast ice because tidal forcing is not considered.

To further improve the simulation of landfast ice, we are currently developing more sophisticated grounding and seabed stress formulations that depend on the ice thickness distribution. Moreover, in this framework, the sea floor is not considered to be flat but is rather expressed based on a probability distribution. As future work, we also plan to study the influence of landfast ice, tides and mixing in the CAA on the export of freshwater to subpolar convective regions.

Acknowledgments

The National Ice Center landfast ice data are available at

http://nsidc.org/data/docs/noaa/g02172_nic_charts_climo_grid/. The CICE-NEMO code and the ECCC atmospheric forcing data used for the numerical experiments are available upon request. The NSIDC sea ice concentration data is available at http://nsidc.org/data/seaice_index/. The ICEsat sea ice thickness data can be obtained at https://nsidc.org/data/icesat.

References

Årthun, M., R. Ingvaldsen, L. Smedsrud, and C. Schrum (2011), Dense water formation and circulation in the Barenas Sea, *Deep Sea Research Part I: Oceanographic Research Papers*, *58*(8), 801 – 817, doi:https://doi.org/10.1016/j.dsr.2011.06.001.

Bouchat, A., and B. Tremblay (2014), Energy dissipation in viscous-plastic sea-ice models, *J. Geophys. Res. Oceans*, *119*(2), 976–994, doi:10.1002/2013JC009436.

Dansereau, V., J. Weiss, P. Saramito, P. Lattes, and E. Coche (2017), Ice bridges and ridges in the maxwell-eb sea ice rheology, *The Cryosphere*, *11*(5), 2033–2058, doi:http://dx.doi.org/10.5194/tc-11-2033-2017.

Dethleff, D., P. Loewe, and E. Kleine (1998), The Laptev Sea flaw lead-detailed investigation on ice formation and export during 1991/1992 winter season, *Cold Reg. Sci. Technol.*, *27*, 225–243.

Divine, D. V., R. Korsnes, A. P. Makshtas, F. Godtliebsen, and H. Svendsen (2005), Atmospheric-driven state transfer of shore-fast ice in the northeastern Kara Sea, *J. Geophys. Res.*, *110*(C09013), doi:10.1029/2004JC002706.

Dumont, D., Y. Gratton, and T. E. Arbetter (2009), Modeling the dynamics of the North Water polynya ice bridge, *J. Phys. Oceanogr.*, *39*, 1448–1461, doi:10.1175/2008JPO3965.1.

Egbert, G. D., and S. Y. Erofeeva (2002), Efficient inverse modeling of barotropic ocean tides, *J. Atmospheric Ocean. Technol.*, *19.2*, 183–204.

Flather, R. A. (1976), A tidal model of the northwest european continental shelf, *Mem. Soc. Roy. Sci. Liege*, *10*, 141–164.

Garric, G., L. Parent, E. Greiner, M. Drévillon, M. Hamon, J.-M. Lellouche, C. Régnier, C. Desportes, O. Le Galloudec, C. Bricaud, Y. Drillet, F. Hernandez, and P.-Y. Le Traon (2017), Performance and quality assessment of the global ocean eddy-permitting physical reanalysis GLORYS2V4., in *EGU General Assembly Conference Abstracts*, *EGU General Assembly Conference Abstracts*, vol. 19, p. 18776.

Haas, C., W. Dierking, T. Busche, and J. Hoelemann (2005), ENVISAT ASAR monitoring of polynya processes and sea ice production in the Laptev Sea, *Tech. rep.*, Alfred Wegener Institute.

Hannah, C., F. Dupont, and M. Dunphy (2009), Polynyas and tidal currents in the Canadian Arctic Archipelago, *Arctic*, *62*, 83–95.

Hibler, W. D. (1979), A dynamic thermodynamic sea ice model, *J. Phys. Oceanogr.*, *9*, 815–846.

Holloway, G., and A. Proshutinsky (2007), Role of tides in arctic ocean/ice climate, *Journal of Geophysical Research: Oceans*, *112*(C4), doi:10.1029/2006JC003643, C04S06.

Hunke, E. C., and W. H. Lipscomb (2008), CICE: the Los Alamos sea ice model. Documentation and software user's manual version 4.0, *Tech. Rep. LA-CC-06-012*, Los Alamos National Laboratory.

Itkin, P., M. Losch, and R. Gerdes (2015), Landfast ice affects the stability of the Arctic halocline: evidence from a numerical model, *J. Geophys. Res.*, *120*(4), 2622–2635, doi:10.1002/2014JC010353.

Johnson, M., A. Proshutinsky, Y. Aksenov, A. T. Nguyen, R. Lindsay, C. Haas, J. Zhang, N. Diansky, R. Kwok, W. Maslowski, S. Häkkinen, I. Ashik, and B. de Cuevas (2012), Evaluation of Arctic sea ice thickness simulated by Arctic Ocean Model Intercomparion Project models, *J. Geophys. Res.*, *117*, C00D13, doi:10.1029/2011JC007257.

Koentopp, M., O. Eisen, C. Kottmeier, L. Padman, and P. Lemke (2005), Influence of tides on sea ice in the Weddell sea: Investigations with a high-resolution dynamic-thermodynamic sea ice model, *J. Geophys. Res.*, *110*, C02,014, doi: 10.1029/2004JC002405.

König Beatty, C., and D. M. Holland (2010), Modeling landfast sea ice by adding tensile strength, *J. Phys. Oceanogr.*, *40*, 185–198, doi:10.1175/2009JPO4105.1.

Laliberté, F., S. E. L. Howell, J.-F. Lemieux, J. Lei, and F. Dupont (submitted), What historical landfast ice observations tell us about projected ice conditions in arctic archipelagoes and marginal seas under anthropogenic forcing, *J. Climate*.

Lemieux, J.-F., L. B. Tremblay, F. Dupont, M. Plante, G. C. Smith, and D. Dumont (2015), A basal stress parameterization for modeling landfast ice, *J. Geophys. Res.*, *120*, 3157–3173, doi:10.1002/2014JC010678.

Lemieux, J.-F., F. Dupont, P. Blain, F. Roy, G. C. Smith, and G. M. Flato (2016), Improving the simulation of landfast ice by combining tensile strength and a parameterization for grounded ridges, *J. Geophys. Res.*, *121*, 7354–7368, doi: 10.1002/2016JC012006.

Lieser, J. L. (2004), A numerical model for short-term sea ice forecasting in the Arctic, *PhD. thesis, Universitat Bremen, Germany.*

Lipscomb, W. H., E. C. Hunke, W. Maslowski, and J. Jakacki (2007), Ridging, strength, and stability in high-resolution sea ice models, *J. Geophys. Res.*, *112*(C03S91), doi:10.1029/2005JC003355.

Locarnini, R. A., A. V. Mishonov, J. I. Antonov, T. P. Boyer, H. E. Garcia, O. K. Baranova, M. M. Zweng, C. R. Paver, J. R. Reagan, D. R. Johnson, M. Hamilton, and D. Seidov (2013), World ocean atlas 2013, volume 1: Temperature., *Tech. rep.*, s. Levitus, Ed., A. Mishonov Technical Ed.; NOAA Atlas NESDIS 73, 40 pp.

Losch, M., and J.-F. Lemieux (submitted), The effect of spatial resolution on the simulated landfast ice cover in an Arctic sea ice-ocean model, *J. Geophys. Res. Oceans*, submitted.

Luneva, M. V., Y. Aksenov, J. D. Harle, and J. T. Holt (2015), The effect of tides on the water mass mixing and sea ice in the Arctic Ocean, *J. Geophys. Res. Oceans*, *120*, 6669–6699, doi:10.1002/2014JC010310.

Madec, G. (2008), *NEMO ocean engine*, Note du Pôle de modélisation, Institut Pierre-Simon Laplace (IPSL), France, No 27, ISSN No 1288-1619.

Mahoney, A., H. Eicken, and L. Shapiro (2007), How fast is landfast sea ice? A study of the attachment and detachment of nearshore ice at Barrow, Alaska, *Cold Reg. Sci. Technol.*, *47*, 233–255, doi:10.1016/j.coldregions.2006.09.005.

Mahoney, A. R., H. Eicken, A. G. Gaylord, and R. Gens (2014), Landfast sea ice extent in the Chukchi and Beaufort Seas: the annual cycle and decadal variability, *Cold Reg. Sci. Technol.*, *103*, 41–56, doi:10.1016/j.coldregions.2014.03.003.

Megann, A., D. Storkey, Y. Aksenov, S. Alderson, D. Calvert, T. Graham, P. Hyder, J. Siddorn, and B. Sinha (2014), GO5.0: The joint NERC-Met Office NEMO global ocean model for use in coupled and forced applications, *Geosci. Model Dev.*, *7*, 1069–1092, doi:10.5194/gmd-7-1069-2014.

National Ice Center (2006, updated 2009), National Ice Center Arctic sea ice charts and climatologies in gridded format, Edited and compiled by F. Fetterer and C. Fowley. Boulder, Colorado USA: National Snow and Ice Data Center, http//dx.doi.org/10.7265/N5X34VDB.

Nihashi, S., and K. I. Ohshima (2015), Circumpolar mapping of Antarctic coastal polynyas and landfast sea ice: relationship and variability, *J. Climate*, *28*(9), 3650–3670, doi: 10.1175/JCLI-D-14-00369.1.

Olason, E. (2016), A dynamical model of Kara Sea land-fast ice, *J. Geophys. Res. Oceans*, doi:10.1002/2016JC011638.

Rabe, B., H. L. Johnson, A. Münchow, and H. Melling (2012), Geostrophic ocean currents and freshwater fluxes across the Canadian polar shelf via Nares Strait, *J.*

Mar. Res., *70*, 603–640, doi:10.1357/002224012805262725.

Rallabandi, B., Z. Zheng, M. Winton, and H. A. Stone (2017), Formation of sea ice bridges in narrow straits in response to wind and water stresses, *J. Geophys. Res. Oceans*, *122*(7), 5588–5610, doi:10.1002/2017JC012822.

Rippeth, T. P., B. J. Lincoln, Y.-D. Lenn, J. A. M. Green, A. Sundfjord, and S. Bacon (2015), Tide-mediated warming of Aarctic halocline by Atlantic heat fluxes over rough topography, *Nature Geosci.*, *8*, 191–944.

Rothrock, D. A. (1975), The energetics of the plastic deformation of pack ice by ridging, *Journal of Geophysical Research*, *80*(33), 4514–4519.

Roy, F., M. Chevallier, G. C. Smith, F. Dupont, G. Garric, J.-F. Lemieux, Y. Lu, and F. Davidson (2015), Arctic sea ice and freshwater sensitivity to the treatment of the atmosphere-ice-ocean surface layer, *J. Geophys. Res. Oceans*, *120*, doi:10.1002/2014JC010677.

Selyuzhenok, V., A. R. Mahoney, T. Krumpen, G. Castellani, and R. Gerdes (2017), Mechanisms of fast-ice development in the southeastern Laptev Sea: a case study for winter of 2007/08 and 2009/10, *Polar Res.*, *36*, doi: https://doi.org/10.1080/17518369.2017.1411140.

Serson, H. V. (1974), Sverdrup channel, *Tech. rep.*, Department of National Defence, Canada. Defence Research Establishment Ottawa., (DREO Tech. Note 72-6).

Smith, G. C., F. Roy, P. Mann, F. Dupont, B. Brasnett, J.-F. Lemieux, S. Laroche, and S. Bélair (2014), A new atmospheric dataset for forcing ice-ocean models: evaluation of reforecasts using the Canadian global deterministic prediction system, *Q. J. R. Meteorol. Soc.*, *140*(680), 881–894, doi:10.1002/qj.2194.

Smith, G. C., F. Roy, M. Reszka, D. Surcel Colan, Z. He, D. Deacu, J.-M. Belanger, S. Skachko, Y. Liu, F. Dupont, J.-F. Lemieux, C. Beaudoin, B. Tranchant, M. Drvillon, G. Garric, C.-E. Testut, J.-M. Lellouche, P. Pellerin, H. Ritchie, Y. Lu, F. Davidson, M. Buehner, A. Caya, and M. Lajoie (2016), Sea ice forecast verification in the Canadian Global Ice Ocan Preduction Sesteem, *Quarterly Journal of the Royal Meteorological Society*, *142*(695), 659–671, doi:10.1002/qj.2555.

Tsamados, M., D. L. Feltham, D. Schroeder, and D. Flocco (2014), Impact of variable atmospheric and oceanic form drag on simulations of Arctic sea ice, *J. Phys. Oceanogr.*, *44*, 1329–1353, doi:10.1175/JPO-D-13-0215.1.

Ungermann, M., L. B. Tremblay, T. Martin, and M. Losch (2017), Impact of the ice strength formulation on the performance of a sea ice thickness distribution model in the Arctic, *J. Geophys. Res. Oceans*, *122*(3), 2090–2107, doi: 10.1002/2016JC012128.

Yu, Y., H. Stern, C. Fowler, F. Fetterer, and J. Maslanik (2014), Interannual variability of Arctic landfast ice between 1976 and 2007, *J. Climate*, *27*, 227–243, doi:10.1175/JCLI-D-13-00178.1.

Zweng, M. M., J. R. Reagan, J. I. Antonov, R. A. Locarnini, A. V. Mishonov, , T. P. Boyer, H. E. Garcia, O. K. Baranova, D. R. Johnson, D. Seidov, and M. M. Biddle (2013), World ocean atlas 2013, volume 2: Salinity., *Tech. rep.*, s. Levitus, Ed., A. Mishonov Technical Ed.; NOAA Atlas NESDIS 74, 39 pp.

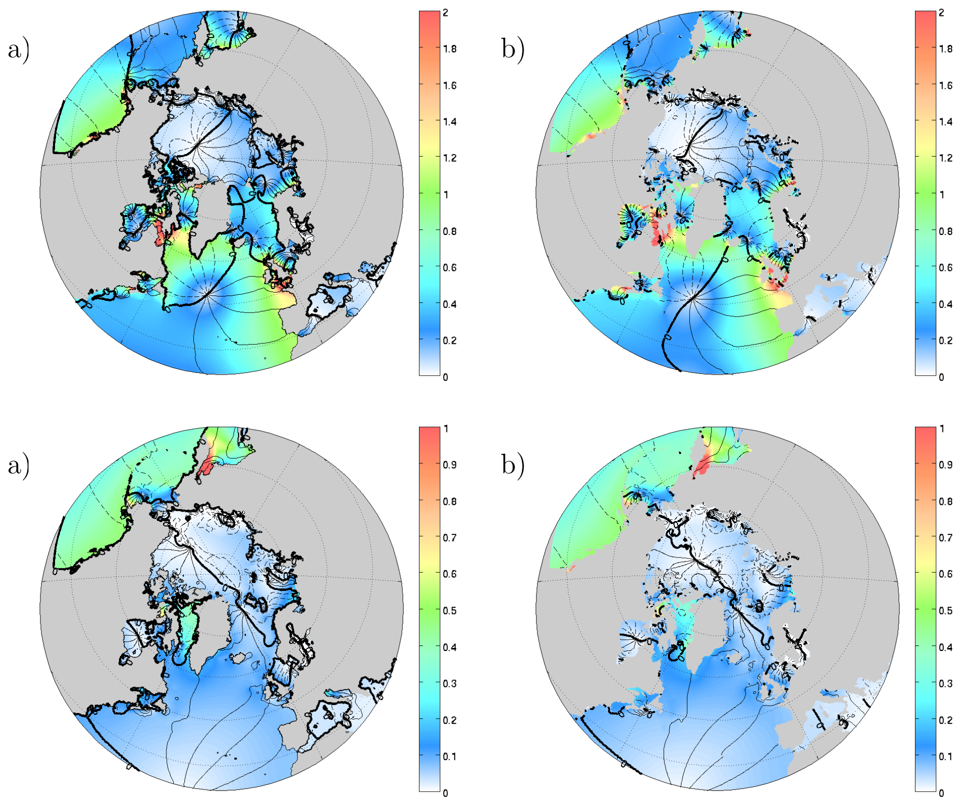

Figure 2. Amplitude (m) and phase of the simulated (a) and OSU reconstructed (b) tidal harmonic M2. Amplitude (m) and phase of the simulated (a) and OSU reconstructed (b) tidal harmonic K1.

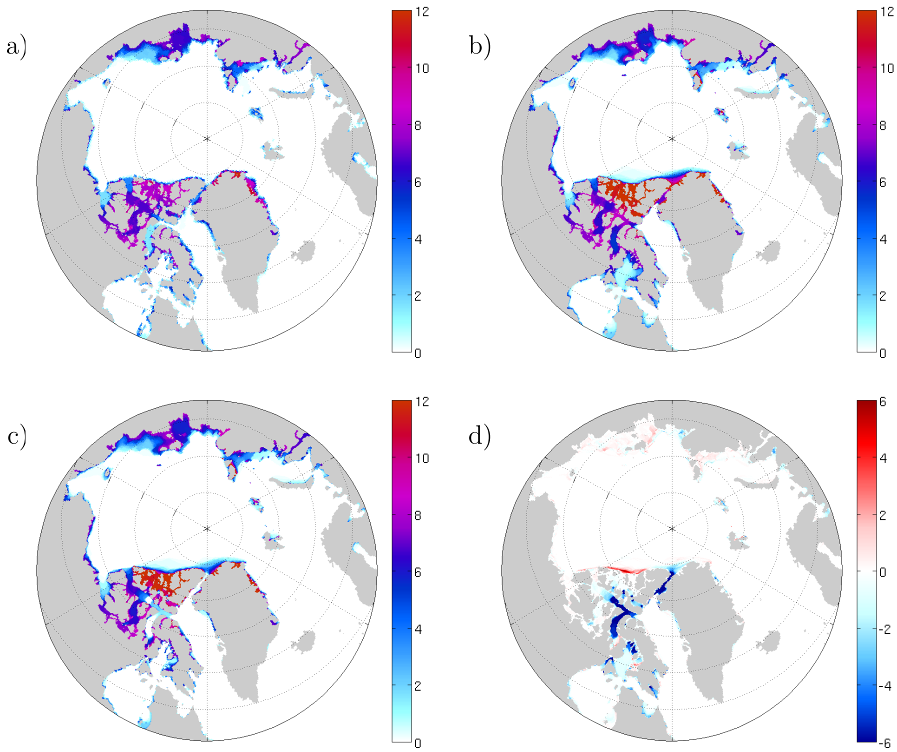

Figure 3. Average number of months of landfast ice, for the period September 2004 to September 2007, for the observations (a), for the NT simulation (b) and for the T simulation (c). The last panel (d) shows the difference between the number of months of landfast ice for the T simulation minus the number of months for the NT one ($N_T - N_{NT}$).

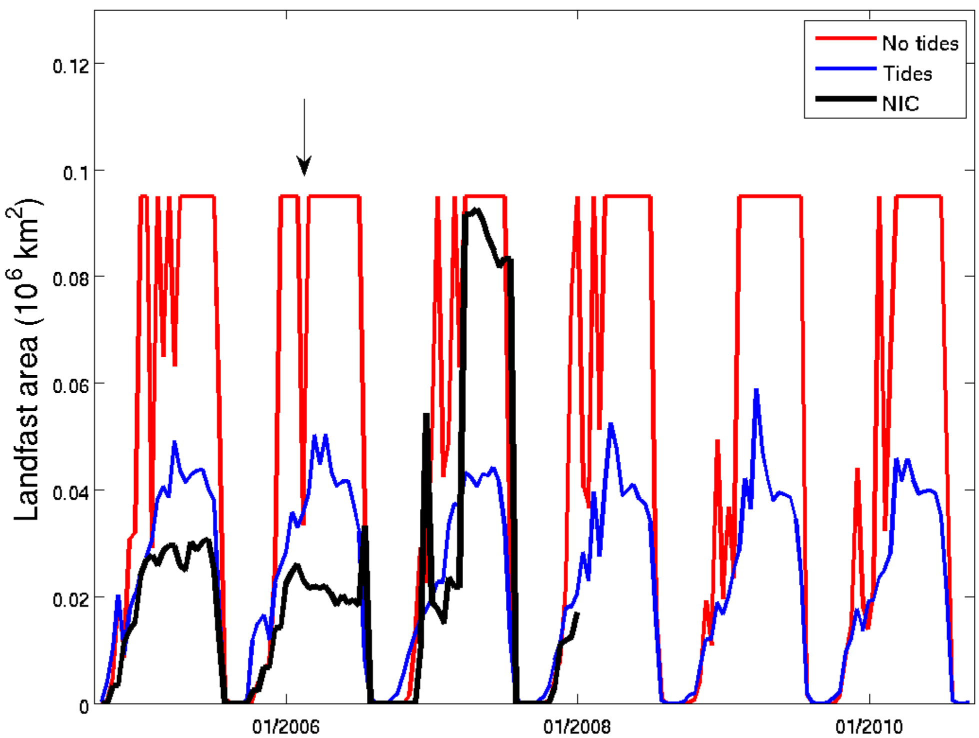

Figure 4. Area of landfast ice in the Boothia region (in yellow in Figure 1) as a function of time for the NT simulation (red), the T simulation (blue) and the NIC data (black). The black arrow indicates a breaking event in the NT simulation that will be discussed. Note that the NIC data ends December 31 2007.

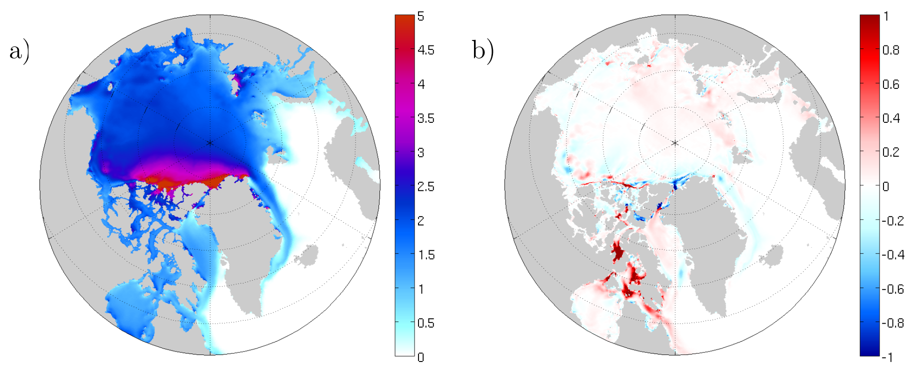

299 **Figure 5.** January-May mean (for the period September 2004 to September 2007) sea ice thickness (m) for the NT simulation (a). T-NT sea ice thickness (b).

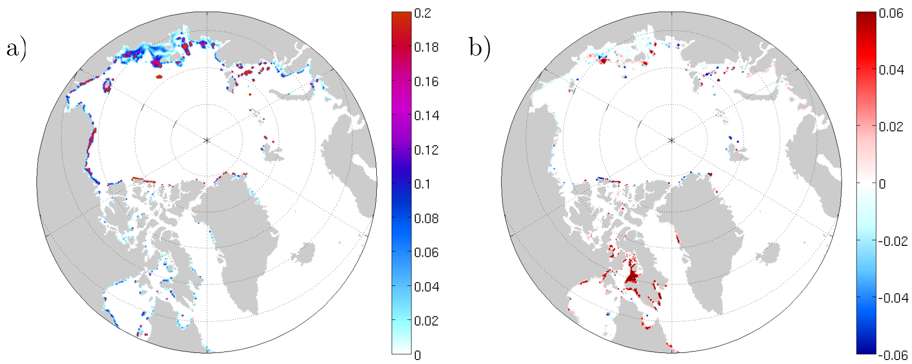

314 **Figure 6.** January-May mean (for the period September 2004 to September 2007) of the
315 magnitude of the basal stress (Nm^{-2}) for the NT simulation (a). T-NT basal stress (b).

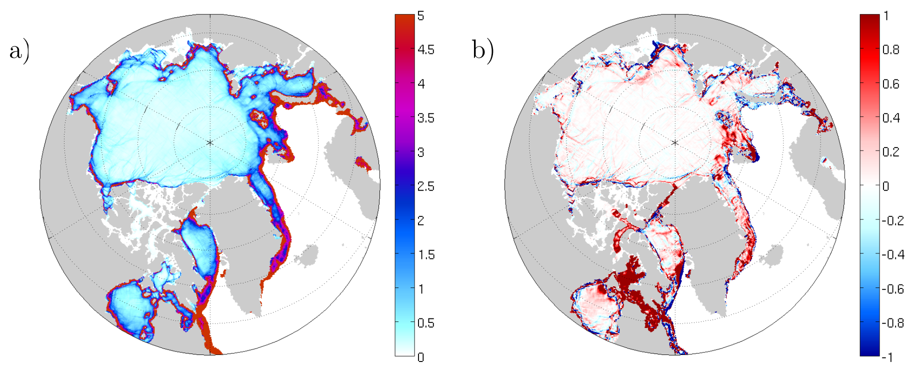

Figure 7. January-May mean (for the period September 2004 to September 2007) absolute ice divergence (day^{-1}) for the NT simulation (a). T-NT absolute divergence (b). Note that these fields were calculated where the January-May mean ice concentration was higher than 0.5.

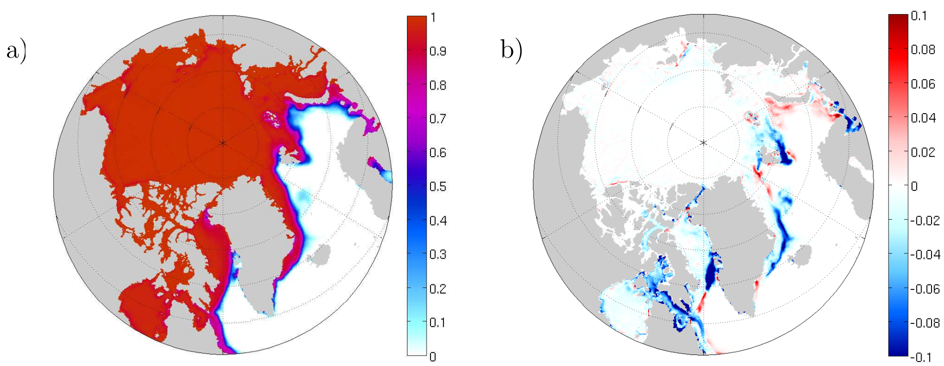

Figure 8. January-May mean (for the period September 2004 to September 2007) sea ice concentration for the NT simulation (a). T-NT sea ice concentration (b).

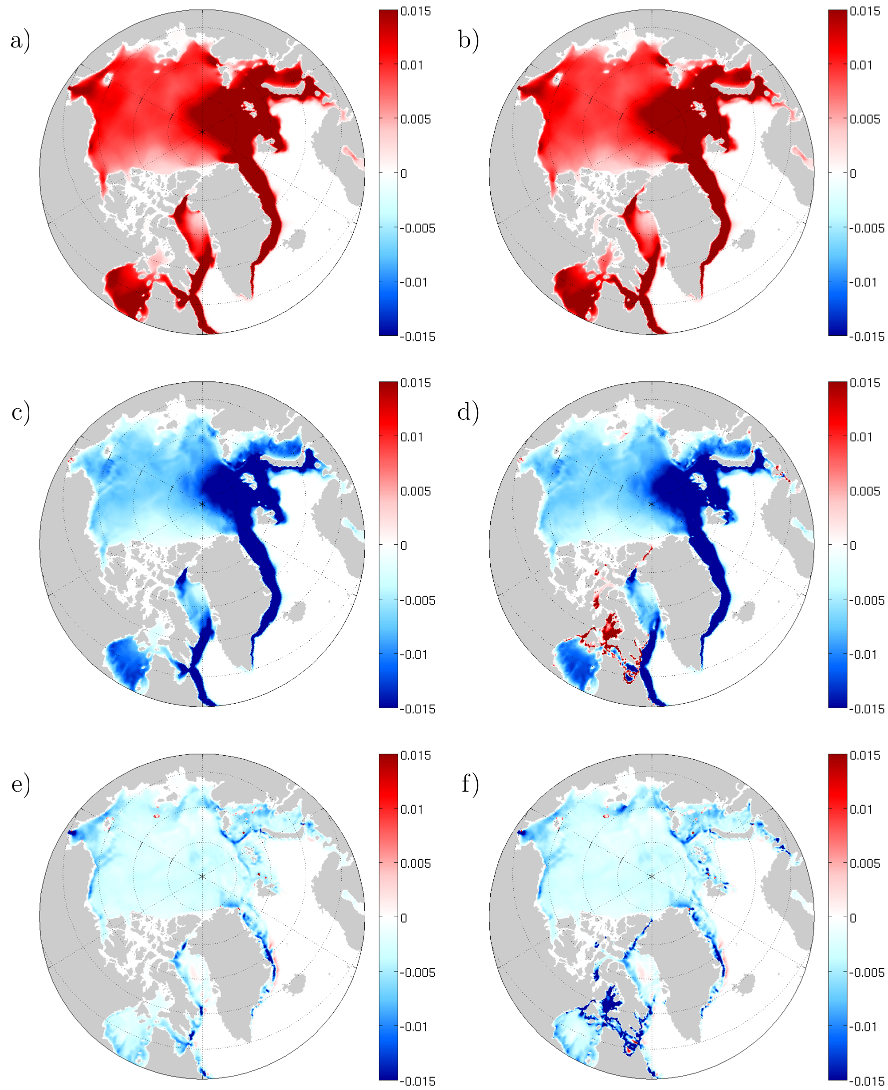

Figure 9. January-May 2006 mean (calculated from hourly outputs) rate of change of kinetic energy (KE) per unit area due to the atmospheric stress term (E_{ai}) for the NT simulation a) and the T simulation b). January-May 2006 mean (calculated from hourly outputs) rate of change of KE per unit area due to the ocean stress term (E_{oi}) for the NT simulation a) and the T simulation b). January-May 2006 mean (calculated from hourly outputs) rate of change of KE per unit area due to the rheology term (E_r) for the NT simulation c) and the T simulation d). Positive (negative) values in red (in blue) indicate that the term provides (removes) KE to the ice cover. The units for the six panels are Wm^{-2}.

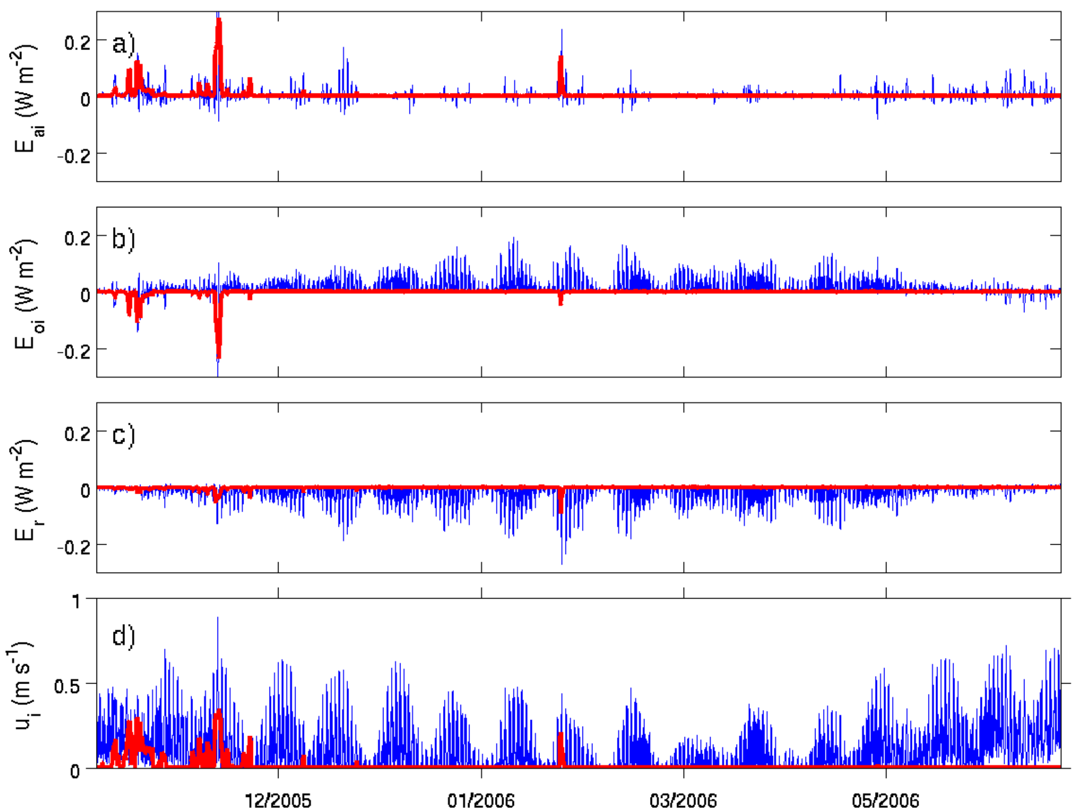

Figure 10. Time series at a point in the Gulf of Boothia of the rate of change of kinetic energy per unit area due the atmospheric stress (a), the ocean stress (b) and the rheology term (c) and time series of the ice speed (d). The NT simulation is in red and the T one is in blue.

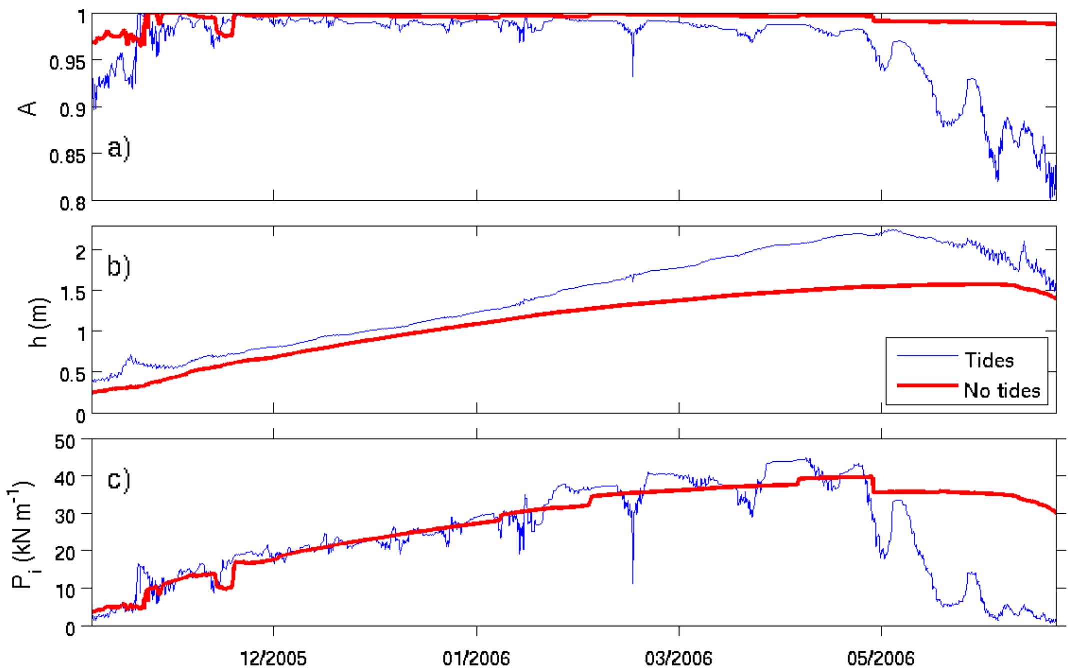

Figure 11. Time series at a point in the Gulf of Boothia of the ice concentration (a), the ice thickness (b) and the ice strength (c). The NT simulation is in red and the T one is in blue.

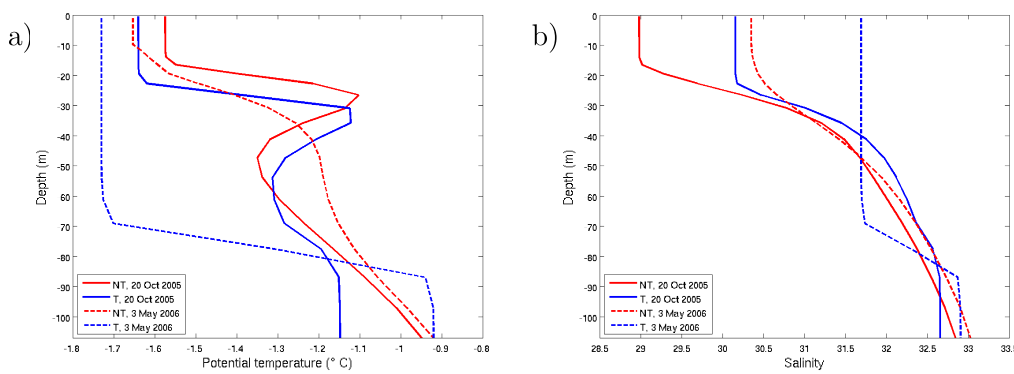

Figure 12. Ocean temperature (a) and salinity (b) profiles at a point in the Gulf of Boothia on 20 October 2005 (solid lines) and on 3 May 2006 (dashed lines) for the NT simulation (in red) and the T simulation (in blue).